J. Fluid Mech. (1999), *vol.* 394, *pp.* 241–260. Printed in the United Kingdom

© 1999 Cambridge University Press

Characteristics of high Rayleigh number two-dimensional convection in an open-top porous layer heated from below

By ABDELLAH S. M. CHERKAOUI AND WILLIAM S. D. WILCOCK

School of Oceanography, University of Washington, Box 357940, Seattle, WA 98195-7940, USA
e-mail: abdul@ocean.washington.edu

(Received 13 July 1998 and in revised form 6 April 1999)

Using a control-volume method and the SIMPLER algorithm, we computed steady-state and time-dependent solutions for two-dimensional convection in an open-top porous box, up to a Rayleigh number of 1100. The evolution of the convective system from onset to high Rayleigh numbers is characterized by two types of transitions in the flow patterns. The first type is a decrease in the horizontal aspect ratio of the cells. We observe two such bifurcations. The first occurs at $Ra = 107.8$ when the convective pattern switches from a steady one-cell roll to a steady two-cell roll. The second occurs at $Ra \approx 510$ when an unsteady two-cell roll evolves to a steady four-cell roll. The second type of transition is from a steady to an unsteady pattern and we also observe two of these bifurcations. The first occurs at $Ra \approx 425$ in the two-cell convective pattern; the second at $Ra \approx 970$ in the four-cell pattern. Both types of bifurcations are associated with an increase in the average vertical convective heat transport. In the bi-cellular solutions, the appearance of non-periodic unsteady convection corresponds to the onset of the expected theoretical scaling $Nu \propto Ra$ and also to the onset of plume formation. Although our highest quadri-cellular solutions show signs of non-periodic convection, they do not reach the onset of plume formation. An important hysterisis loop exists for Rayleigh numbers in the range 425–505. Unsteady convection appears only in the direction of increasing Rayleigh numbers. In the decreasing direction, steady quadri-cellular flow patterns prevail.

1. Introduction

Thermal convection at high Rayleigh numbers in porous media is a subject of considerable interest in contemporary fluid flow and heat transfer research. Its importance stems from a wide range of occurrences in industrial applications and geological systems. From a purely scientific point of view, porous convection is also of great interest because it is one of the simplest systems exhibiting nonlinear instability. The evolution of convective patterns from stationary to chaotic and its effect on the overall heat transport as the Rayleigh number increases, has been studied for many configurations (e.g. Nield & Bejan 1992). Surprisingly, very little work has been done on thermal convection in open-top porous layers heated from below, a configuration of significant importance in marine geophysics. Convective flow of seawater on the ocean floor accounts for nearly a quarter of the Earth's total heat budget (Williams & Von Herzen 1986; Stein & Stein 1994) and is the dominant mechanism by which newly formed oceanic crust cools. A third of this heat loss occurs at mid-ocean ridges,

the locus of formation for the oceanic lithosphere and the site of 70% of the Earth's volcanism. Here, general absence of a sediment cover allows free flow of fluid in and out of the crust, and high permeabilities coupled with high basal temperatures result in very vigorous convection with Rayleigh numbers up to 10^4 and perhaps higher (Lister 1981; Wilcock & Delaney 1996). The highest temperature vent sites generally lie on the ridge axis and at many locations it is believed that deep circulation is primarily two-dimensional (e.g. Haymon 1996). Extensional tectonism at the spreading boundary produces a narrow zone of high and very anisotropic permeability (e.g. Fisher 1998) where most of the flow may be confined. A study of two-dimensional porous convection in an open-top system at high Rayleigh numbers is thus a natural first step towards understanding the basic configuration of high-temperature circulation at mid-ocean ridges.

Both laboratory and numerical investigations of convection in a confined porous medium have established the existence of transitions from steady to time-periodic motions. Combarnous & LeFur (1969) first inferred such a transition from observations of a 'fluctuating' state in porous convection experiments. Further observations in saturated porous beds (Caltagirone, Cloupeau & Combarnous 1971) and in Hele-Shaw cells (Lyubimov, Putin & Chernatynskii 1977; Koster 1982, 1988; Koster & Muller 1984; Graham, Muller & Steen 1992) showed that higher transitions exist within the time-periodic regime.

Numerical studies of confined systems are more numerous than their laboratory counterpart. Motivated by the observations of Combarnous & LeFur (1969) and of Caltagirone *et al.* (1971), Caltagirone (1975) determined the stability curve of steady convection as a function of the aspect ratio of a rectangular container using a Galerkin technique. Solving many initial-value problems with a finite-difference scheme, he obtained the structure of the fluctuating patterns above the stability boundary without resolving the detailed structure or reporting wavenumbers or frequencies. Horne & O'Sullivan (1974, 1978) use a finite-difference technique and suggest that the convective oscillations arise from interactions between an unstable bottom layer and descending cold disturbances. Horne & Caltagirone (1980) find that the point of origin of the instability in the thermal boundary layer determines whether the oscillating state is periodic or irregular.

More recent numerical work (Schubert & Straus 1982; Kimura, Schubert & Straus 1986; Aidun 1987; Aidun & Steen 1987; Caltagirone, Fabrie & Combarnous 1987; Steen & Aidun 1988; Caltagirone & Fabrie 1989; Graham & Steen 1992, 1994) has been primarily concerned with uncovering routes to chaos in the context of porous-media convection. Using spectral methods, these studies determine more accurately the Rayleigh number and the frequency of oscillations at the transition to time-dependence and at a sequence of higher transitions. For a square cross-section the convective states evolve with Rayleigh number through the sequence: Steady S – periodic P^1 – quasi-periodic QP – periodic P^2. Although these studies agree closely below $Ra = 600$, some discrepancies appear at higher Rayleigh numbers. For instance Kimura *et al.* (1986) observe a discontinuity in the P^2 state around $Ra = 625$–640, coinciding with a second small window of quasi-periodicity. Caltagirone & Fabrie (1989) interpret it as a result of frequency locking but this is inconsistent with the observed frequency spectra of Kimura *et al.* (1986). Graham & Steen (1992) resolve this discrepancy by studying the interactions between the Hopf bifurcations from the steady roll which they consider as travelling waves. In a recent study of the confined system, Graham & Steen (1994) show that boundary-layer fluctuations born at a Hopf bifurcation and convected by the steady circulation eventually develop into thermal

plumes. The appearance of plumes corresponds to the onset of the classical boundary-layer scaling laws first proposed by Howard (1964) for Rayleigh–Bénard convection at high Rayleigh number. They also show that, at higher Rayleigh numbers, plume formation is disturbed by instabilities resulting from the interactions between the top and bottom thermal boundary layers.

In contrast to the confined configuration, very little work has been done on the open-top porous layer heated from below, particularly at high Rayleigh numbers. A few analytical and numerical results exist for the onset of convection and its characteristics at low Rayleigh numbers (Donaldson 1962; Nield 1968; Ribando, Torrance & Turcotte 1976; Rosenberg 1991). In an attempt to determine the importance of the interactions between hot and cold disturbances relative to thermal boundary layer instabilities, Horne & O'Sullivan (1978) computed solutions for unsteady convection in a porous rectangle with a permeable top. Their results revealed several basic differences from the closed system. There are no descending thermal disturbances and the downwelling fluid is almost entirely cold. The ascending disturbances evolve with similar frequencies but have greater amplitudes and velocities than the closed system counterparts. The Rayleigh number at which the oscillatory flow first appears is somewhat lowered. They conclude that oscillatory flow is an inherent property of the unstable boundary layer above the heated surface. However, their results are based on a partially heated bottom, a boundary condition which maintains a regularly fluctuating unicellular regime at Rayleigh numbers above 480 (Horne & O'Sullivan 1974).

In this study we investigate the evolution of the flow and heat transport patterns, from the onset of convection to high Rayleigh numbers, in an open-top porous square uniformly heated from below. In the next section, we briefly discuss the mathematical formulation of the problem and outline the numerical procedure used in its solution. Section 3 contains the results of a benchmark of our numerical model. In § 4, we describe the numerical results. We give the Rayleigh numbers for the transitions in the convective patterns up to the limit of resolution of our numerical scheme, describe the characteristics of the convective patterns after each transition, and analyse their effects on the heat transport. In § 5 we discuss the more general aspects of the numerical results. Section 6 concludes with a summary of the important results of this study.

2. Model formulation

2.1. *Governing equations*

We consider a bounded two-dimensional square porous layer of thickness H. The vertical boundaries are adiabatic and impermeable. The horizontal boundaries are isothermal. The temperature difference across the porous layer is ΔT; the porous layer is heated from below. The bottom is impermeable while the top is permeable and at a constant pressure. The porous medium has a porosity ϕ, a permeability K, a heat capacity $(\rho c)_s$ and is saturated with an incompressible fluid which has a constant dynamic viscosity μ, a coefficient of thermal expansion α, a density ρ and a heat capacity $(\rho c)_f$. The thermal conductivity of the fluid-saturated porous medium is λ. We use the Boussinesq approximation and assume the flow obeys Darcy's law and that inertial terms can be neglected (i.e. the permeability K of the medium is small). Under these conditions the equations governing flow within the porous layer are

$$\nabla \cdot \boldsymbol{v} = 0, \tag{2.1}$$

$$\boldsymbol{v} = \frac{\boldsymbol{K}}{\mu}(-\nabla p + \rho \boldsymbol{g}), \tag{2.2}$$

$$(\phi(\rho c)_f + (1-\phi)(\rho c)_s)\frac{\partial T}{\partial t} + (\rho c)_f \boldsymbol{v} \cdot \nabla T = \lambda \nabla^2 T, \tag{2.3}$$

$$\rho = \rho_c(1 - \alpha(T - T_c)), \tag{2.4}$$

where $\boldsymbol{v}$ is the Darcy velocity and $\boldsymbol{g}$ is the acceleration due to gravity. Since ϕ is small for most real systems, the energy equation (2.3) can be reduced to

$$\sigma\frac{\partial T}{\partial t} + \boldsymbol{v} \cdot \nabla T = \kappa \nabla^2 T, \tag{2.5}$$

where $\sigma = (\rho c)_s/(\rho c)_f$ is typically near unity (Bear 1972) and κ is the thermal diffusivity of the fluid-saturated porous medium. The problem is non-dimensionalized by scaling lengths with H, time with H^2/κ, temperature with ΔT, velocities with κ/H and pressure with $\kappa\rho_c/\mu K$. Keeping the same notation for all the variables and assuming $\sigma = 1$, the dimensionless equations are

$$\nabla \cdot \boldsymbol{v} = 0, \tag{2.6}$$

$$\boldsymbol{v} = -\nabla p + Ra T \cdot \boldsymbol{k}, \tag{2.7}$$

$$\frac{\partial T}{\partial t} + \boldsymbol{v} \cdot \nabla T = \nabla^2 T, \tag{2.8}$$

where the Rayleigh number $Ra = K\alpha\rho_c g H \Delta T/\mu\kappa$ is a dimensionless parameter determining the vigour of convection within the porous layer. The boundary conditions are

$$\left.\begin{aligned} T(x,0) &= 1; \quad T(x,1) = 0, \\ \frac{\partial T}{\partial x}(0,z) &= \frac{\partial T}{\partial x}(1,z) = 0, \\ u(0,z) &= u(1,z) = 0, \quad w(x,0) = 0, \quad p(x,1) = 0. \end{aligned}\right\} \tag{2.9}$$

In addition to the Rayleigh number, it is useful to introduce other global measures of convective vigour (e.g. Lennie *et al.* 1988; Rosenberg 1991). One such quantity is the total kinetic energy

$$KE = \frac{1}{2}\int_0^1 \int_0^1 (u^2 + w^2)\mathrm{d}x\,\mathrm{d}z, \tag{2.10}$$

where u and w are the horizontal and vertical components of the velocity vector $\boldsymbol{v}$, respectively. Another is the Nusselt number Nu, which provides a dimensionless measure of the heat flux across the porous medium. For a layer heated entirely from below

$$Nu = -\int_0^1 \left.\frac{\partial T}{\partial z}\right|_{z=0} \mathrm{d}x \tag{2.11}$$

and is the ratio of the observed heat flux to that in the absence of convection. Since $Nu = 1$ when no motion exists, $(Nu - 1)$ is the dimensionless convective heat flux. Finally, we define the horizontal aspect ratio of a convective cell as $A = L/H$ where L is the width of the cell.

2.2. *Solution methodology*

Equations (2.6) to (2.8), together with the boundary conditions (2.9) are solved using a second-degree-accurate finite-volume method based on the SIMPLER algorithm

(Patankar 1980, 1981). We outline this method briefly below (see Patankar 1980 for a detailed discussion). Each of the differential equations can be cast into the general balance equation form

$$\frac{\partial(\rho\phi)}{\partial t} + \nabla \cdot \left[\rho \boldsymbol{v}\phi - \Gamma_\phi \cdot \nabla\phi\right] = S_\phi, \tag{2.12}$$

where ϕ denotes any one of the independent variables, Γ_ϕ an exchange coefficient and S_ϕ a source term. Once in this form, the balance equations are integrated over control volumes defined on a staggered grid. The transient term is treated with an implicit backward difference and the momentum fluxes across the control surfaces are evaluated approximately with an exponential scheme. The boundary conditions are introduced as source terms in the cells neighbouring boundaries. The resulting system of algebraic equations is solved using an iterative line-by-line method. The sequence of operations is as follows:

(i) guess an initial pressure field;

(ii) solve the momentum equations, thereby obtaining velocities which satisfy momentum but not continuity;

(iii) calculate mass imbalance for each control volume;

(iv) solve a pressure correction equation;

(v) adjust the pressure and velocity fields, obtain velocities which satisfy continuity, but not momentum;

(vi) iterate back to step (ii), using the new pressure field, until both errors on continuity and momentum satisfy the convergence criterion.

This method is extremely stable and reduces the possibility of round-off errors affecting the solution. To improve the relatively long convergence times induced by the line-by-line method we use an inertial relaxation method by introducing a false-time step in the source terms of the energy and the momentum equations as described by Patankar (1980). To further improve the accuracy and convergence rates of our solutions we use a non-uniform grid. In the vertical direction, the width $\mathrm{d}z_i$ of the ith of n_z cells varies according to the power law

$$\mathrm{d}z_i = (i/n_z)^p. \tag{2.13}$$

The mesh is uniform in the horizontal direction. We used grid refinement techniques to determine the optimal grid configuration, time step and relaxation parameters. All the solutions presented hereinafter were obtained using a mesh of 64×64 control cells except for the time-dependent solutions above $Ra = 900$ which were computed with 96×96 control cells. In both cases we used a power $p = 1.2$ to get an optimal resolution of the bottom boundary layer with respect to the total number of cells used. The time step is 10^{-6} for all the time-dependent solutions presented. Doubling the mesh size and decreasing the time step ten-fold did not affect the solution by more than 3% with respect to the average Nusselt number and the spectral characteristics for test cases at $Ra = 490$ and 1000.

3. Test case: convection in a closed layer

We have previously used this numerical scheme successfully to solve Darcy flow problems at high Rayleigh numbers with a vertical heat source (Cherkaoui, Wilcock and Baker 1997). However, when seeking to evaluate how well our numerical code can resolve the small-scale instabilities responsible for unsteady convection in a porous layer heated from below, we were confronted by the lack of published results for

Ra	Nusselt number, *Nu*		
	This paper	Caltagirone (1975)	Steen & Aidun (1988)
50	1.450	1.44	1.450
100	2.647	2.65	2.651
150	3.324	3.32	—
200	3.801	3.81	3.810
250	4.195	4.19	4.199
300	4.519	4.52	4.523
350	4.786	4.79	—

TABLE 1. Comparison of the Nusselt number of closed-top solutions for steady convection.

	This paper			Kimura *et al.* (1986)			Caltagirone & Fabrie (1989)			Graham & Steen (1994)	
Ra	*Nu*	f_1	f_2	Nu^*	f_1^*	f_2^*	*Nu*	f_1	f_2	Nu^*	f_1
500	5.82	100.2	28.0	5.9	—	—	5.86	101.5	28.2	—	—
540	6.03	108.1	29.6	6.1	110	30	6.07	111.0	30.8	—	—
800**	9.14	299.7	—	9.3	280	—	9.42	296.0	—	9.0	285

* These values were read from graphs in the article.
** The regime is single-periodic at $Ra = 800$ (figure 1).

TABLE 2. Comparison of the average Nusselt number and the characteristic frequencies f_1 and f_2 for unsteady convection in closed-top solutions.

the open-top case. In order to benchmark our numerical model, we first obtained solutions to equations (2.6) to (2.8) subject to the closed-top boundary conditions (e.g. Kimura *et al.* 1986; Steen & Aidun 1988; Caltagirone & Fabrie 1989; Graham & Steen 1994):

$$\left.\begin{aligned} T(x,0) &= 1; \quad T(x,1) = 0, \\ \frac{\partial T}{\partial x}(0,z) &= \frac{\partial T}{\partial x}(1,z) = 0, \\ u(0,z) &= u(1,z) = 0, \quad w(x,0) = w(x,1) = 0. \end{aligned}\right\} \tag{3.1}$$

We obtained both time-independent and time-dependent solutions for Rayleigh numbers in the range 0–800 (tables 1 and 2). Our model predicts correctly the onset of convection at $Ra = 39.5$. From this first bifurcation up to $Ra \approx 390$, the flow is steady and the intensity of the convective motion increases with the Rayleigh number. Our results match closely those of Caltagirone (1975) and Steen & Aidun (1988) (table 1). Above $Ra \approx 395$, time-dependent solutions become unsteady and progressively begin to differ from the time-independent solutions. The time-independent solutions are real mathematical solutions but are physically unstable. For $Ra = 500$, 540 and 800 we computed solutions over periods of time long enough to yield meaningful temporal characteristics (table 2). The average Nusselt numbers compare well with those of Kimura *et al.* (1986); Caltagirone & Fabrie (1989) and Graham & Steen (1994). At $Ra = 500$ and 540, our numerical model predicts correctly the existence of two incommensurable frequencies f_1 and f_2 in the energy spectrum of the Nusselt number. Our numerical models also resolves the subsequent return to a simply pe-

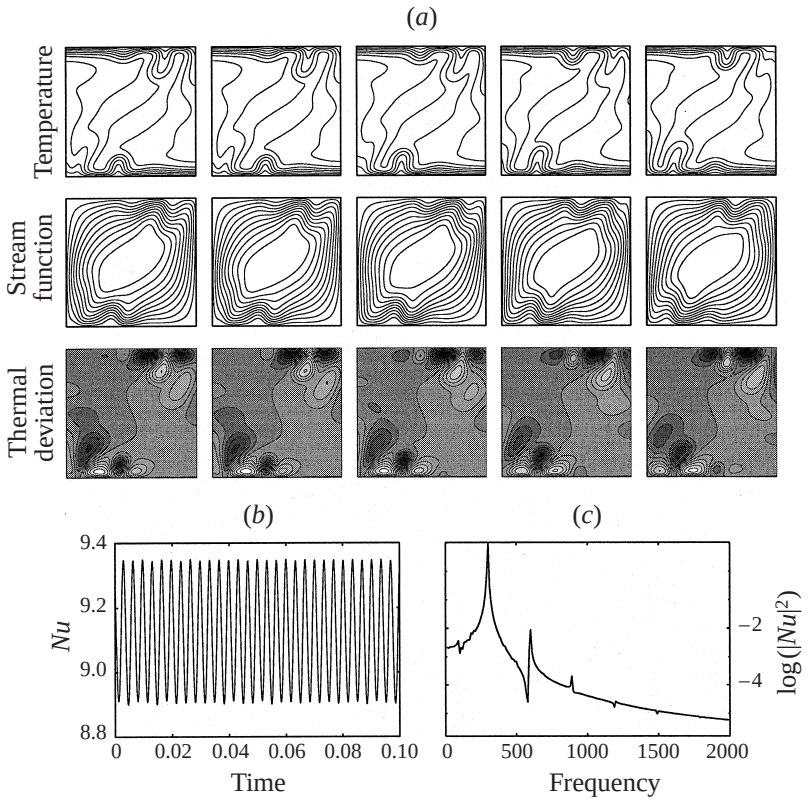

FIGURE 1. Unsteady convection in a closed box at $Ra = 800$. (*a*) Evolution of the temperature, stream function and iso-disturbances over one oscillatory cycle. The iso-disturbances are obtained by subtracting the average temperature field from the temperature. Temperature is contoured every 0.1 unit from 0.1 to 0.9. There are ten equally spaced stream function contours. For the iso-disturbances, dark shades represent positive anomalies. The maximum anomalies are close to 0.3. (*b*) Nusselt number as a function of time. (*c*) Power spectrum of the Nusselt number. Only one fundamental frequency $f_1 = 299.7$ prevails at $Ra = 800$, versus two at $Ra = 500$ and $Ra = 540$. These results match closely the results of recent numerical studies (e.g. Kimura *et al.* 1986; Caltagirone & Fabrie 1989; Graham & Steen 1992). The temporal characteristics are in close (6% or less) agreement with previously published results (table 1).

riodic regime at higher Rayleigh number predicted by Graham & Steen (1994) and others. For instance, at $Ra = 800$ (figure 1), our numerical solution is characterized by one prevailing frequency, in close agreement with previously published results. The power spectrum of the Nusselt number shows no broadband noise, which is usually characteristic of single periodic regimes (e.g. Gollub & Benson 1980; Baker & Gollub 1996). Overall, these results suggest that our numerical model will provide accurate solutions to the open-top problem.

4. Results

We computed solutions to the open-top problem (equations (2.6) to (2.8) with boundary conditions (2.9)) for Ra in the range 0–1100. We started initially with a motionless fluid and a conductive temperature gradient across the box, and increased the Rayleigh number incrementally. We obtained both time-dependent and time-

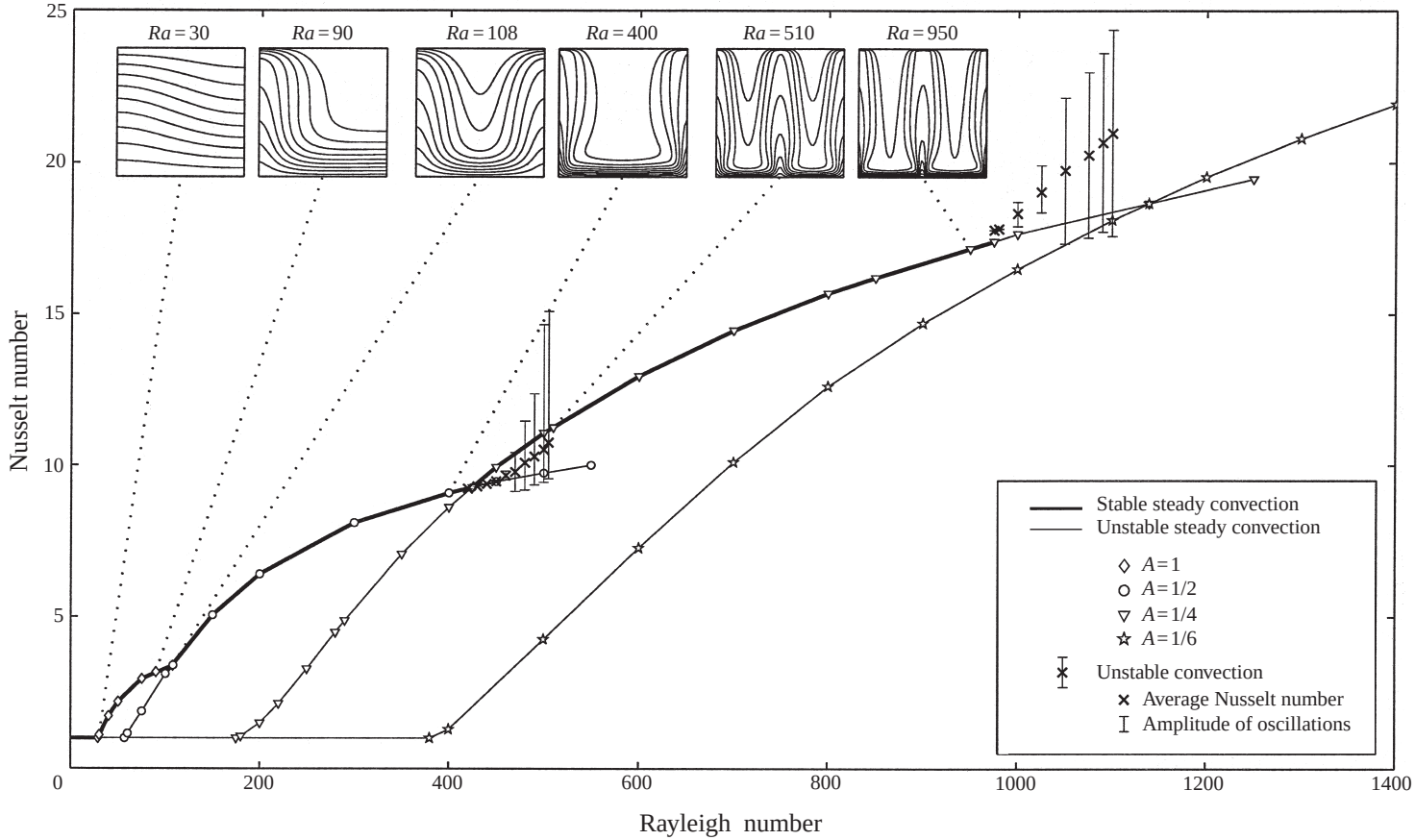

FIGURE 2. For caption see facing page.

independent solutions (i.e. with and without the transient term of equation (2.8)) and summarize all results with respect to the Nusselt number (figure 2). We observe several transitions which modify significantly the characteristics of the flow and the heat transport. These transitions can involve a change in the aspect ratio of the convective cells, a change from steady to unsteady flow patterns or a change from unsteady to steady flow patterns.

4.1. *First transition: onset of convection*

The minimum critical Rayleigh number for the onset of convection in an infinite open-top porous layer confined between two isothermal horizontal boundaries is 27.1 (Nield 1968). The corresponding flow pattern just above onset is a single convective cell with a natural aspect ratio (width/height) of 1.35. In the square configuration, the vertical boundaries force the aspect ratio of the convective cell above onset to be 1. In that case, we determine the critical Rayleigh number to be 29.3. Above onset, the flow is steady and the convective motion increases in intensity with the Rayleigh number (figure 2). The bottom boundary layer develops as a prominent feature of the flow and temperature fields. As convection becomes the dominant mechanism of heat transport, the evolution of the flow with increasing Ra is characterized by a narrowing of the upwelling plume and broadening of the downwelling area. The total kinetic energy increases at an approximately constant rate (figure 3*a*), in contrast with the Nusselt number whose rate of increase declines with increasing Ra (figure 2).

4.2. *Second transition: steady-to-steady bifurcation from* $A = 1$ *to* $A = \frac{1}{2}$

We can obtain one-cell convective solutions to the time-independent problem up to $Ra = 105$ (figure 2). At higher values, converged solutions display a two-cell convective pattern. We resolve the exact point of the transition using Newton's iteration method. Mono-cellular steady states can be obtained up to $Ra = 107.8$. We obtained solutions to the time-dependent problem for $Ra = 110$, 125 and 150, starting each simulation with the monocellular solution at $Ra = 100$ (figures 4*a*, 4*b*). The evolution of the flow and temperature distributions is analogous to the initial onset of convection. The boundary layer becomes unstable and a new upwelling site develops, creating two cells of aspect ratio 0.5. The transformation time from an initial one-cell pattern at $Ra_1 = 100$ to a two-cell pattern at a Rayleigh number Ra_2 greater than 107.8 increases rapidly as Ra_2 is brought closer to Ra_1 (figure 4*b*). Although the flow patterns undergo a fundamental change across the transition, it is interesting to note that the projection of the solutions onto the kinetic energy–Nusselt number plane are very close (figure 4*c*). A mixed mode could exist just above $Ra \approx 107.8$ but our numerical approach does not lend itself well to resolving the exact nature of this transition. We also obtained time-dependent solutions for $Ra_2 = 50$ and 100, starting each with the bi-cellular solution at $Ra_1 = 125$. The flow patterns

FIGURE 2. Evolution of the Nusselt number as a function of the Rayleigh number in an open-top square. Each branch corresponds to a different aspect ratio A (width/height) of the convective cells: diamonds, circles, triangles and pentagrams show solutions to the time-independent problem. Crosses show time-dependent solutions which differ from the time-independent ones (i.e. unsteady convection). At a given Rayleigh number only one solution is stable (bold line and crosses) except between $Ra = 425$ and $Ra = 505$ where a hysteresis loop exists and two stable solutions can be obtained. Unsteady bi-cellular solutions are realized in the increasing-Ra direction while steady quadri-cellular solutions prevail in the decreasing direction. The insets show temperature contours solutions (contoured every 0.1 unit from 0.1 to 0.9) from each of the three flow configurations realized in the open-top square.

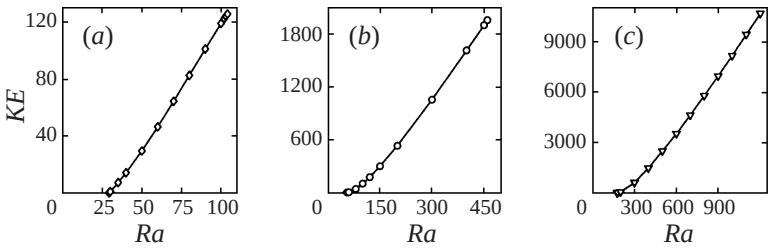

FIGURE 3. Total kinetic energy of steady solutions as a function of the Rayleigh number for solutions with aspect ratios A (width/height) of (a) 1, (b) $\frac{1}{2}$, (c) $\frac{1}{4}$.

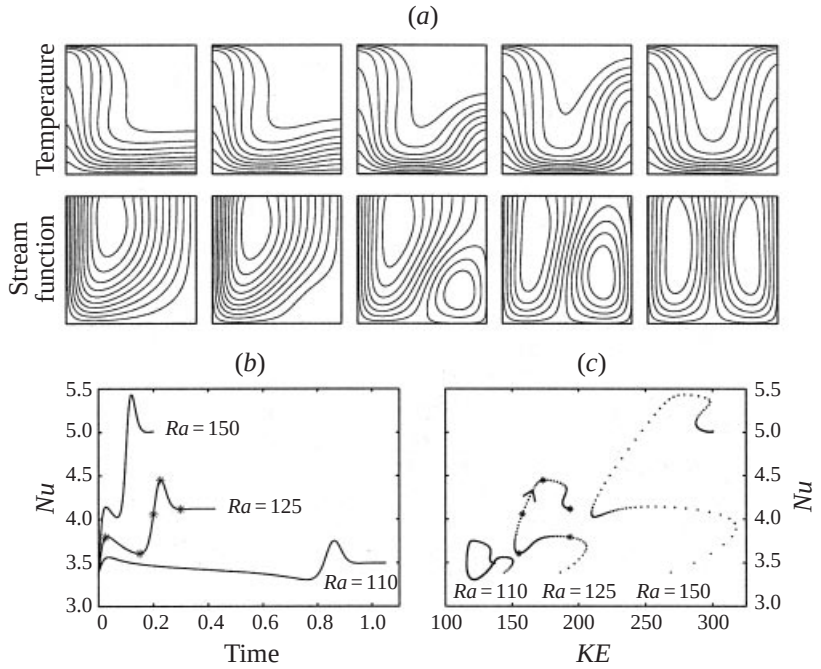

FIGURE 4. Evolution of the convective system across the transition from a steady one-cell pattern to a steady two-cell pattern. Time-dependent solutions are computed for $Ra = 110$, 125 and 150, starting with the solution at $Ra = 100$. (a) Snapshots of the stream function and temperature for the solution at $Ra = 125$. Temperature contouring is identical to figure 2. There are ten equally spaced stream function contours. (b) Nusselt number as a function of time. (c) Nusselt number as a function of the total kinetic energy. Stars mark the location of the snapshots shown in (a).

return to a single-cell configuration showing that the mono-cellular solutions are the stable ones below $Ra = 107.9$. Bi-cellular flow patterns can still be obtained below $Ra = 107.9$ by solving the time-independent problem starting with initial solutions above $Ra = 107.9$ and decreasing the Rayleigh number by small decrements. We infer that such solutions are mathematically correct but physically unstable.

Above the transition, the evolution of the flow patterns is similar to the mono-cellular solutions. The thermal boundary layer sharpens while the upwelling plumes narrow (figure 2). The total kinetic energy increases linearly (figure 3b), while the Nusselt number's rate of increase declines with increasing Rayleigh number (figure 2).

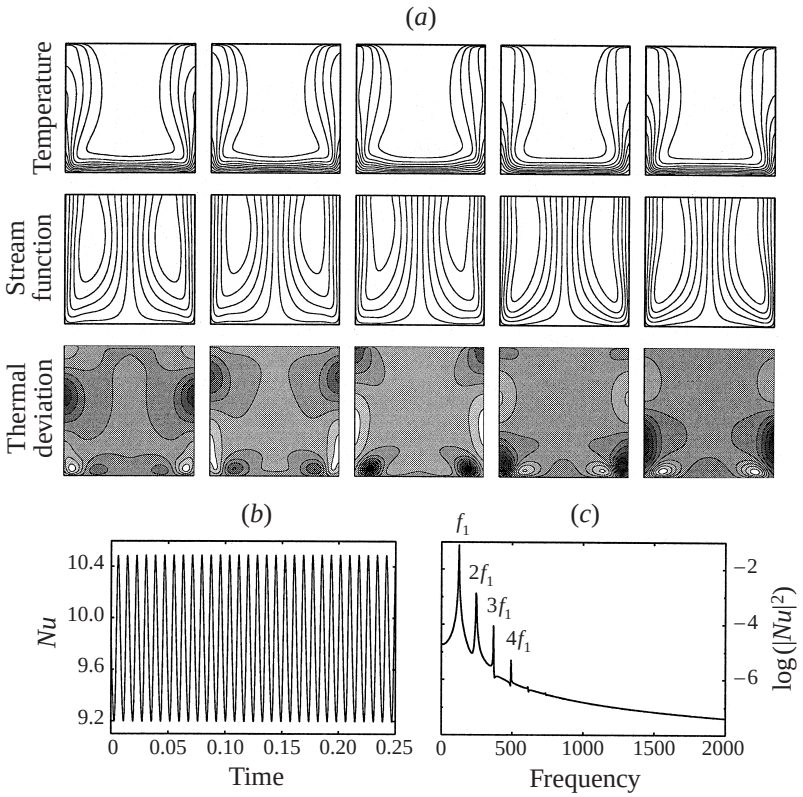

FIGURE 5. Temporal characteristics of unsteady convection at $Ra = 470$. (*a*) Snapshots of the temperature, stream function and iso-disturbances over one oscillation. Contouring is identical to figure 1(*a*), Maximum anomalies correspond here to a temperature difference of 0.11. At $Ra = 470$ a single frequency, $f_1 = 117.2$, and its harmonics prevail. Constant-size instabilities appear regularly within the thermal boundary layer and are split symmetrically by the bicellular convective flow.

4.3. *Third transition: steady-to-unsteady bifurcation at* $A = \frac{1}{2}$

The earliest detectable unsteady flow patterns appear above $Ra \approx 425$. The first trace of unsteadiness are very small, periodic oscillations in the Nusselt number with a single frequency $f_1 \approx 101$. The amplitude of the oscillations increases sharply with the Rayleigh number, reaching 12% of the average at $Ra = 470$ (figure 5). The evolution of the temperature field, the streamlines and the iso-disturbances (deviations from the average temperature field) show the instabilities responsible for unsteady convection. They arise at the centre of the thermal boundary layer and are then split in half and convected symmetrically towards the vertical walls. Their characteristic frequency is $f_1 = 117.2$ (figure 5*c*). The periodicity of the oscillations in the Nusselt number is a direct consequence of the constant frequency of appearance and size of the thermal instabilities.

The convective system departs from this single-periodic state at $Ra = 480$, when a second fundamental frequency $f_2 = 20.2$, incommensurable with $f_1 = 123.9$, appears in the power spectrum. Snapshots of the temperature field, streamlines and iso-disturbances at $Ra = 490$ (figure 6) show that the loss of periodicity results from uneven splitting of the instabilities developing in the central part of the boundary layer. Larger instabilities now flow alternately along the right and left walls and

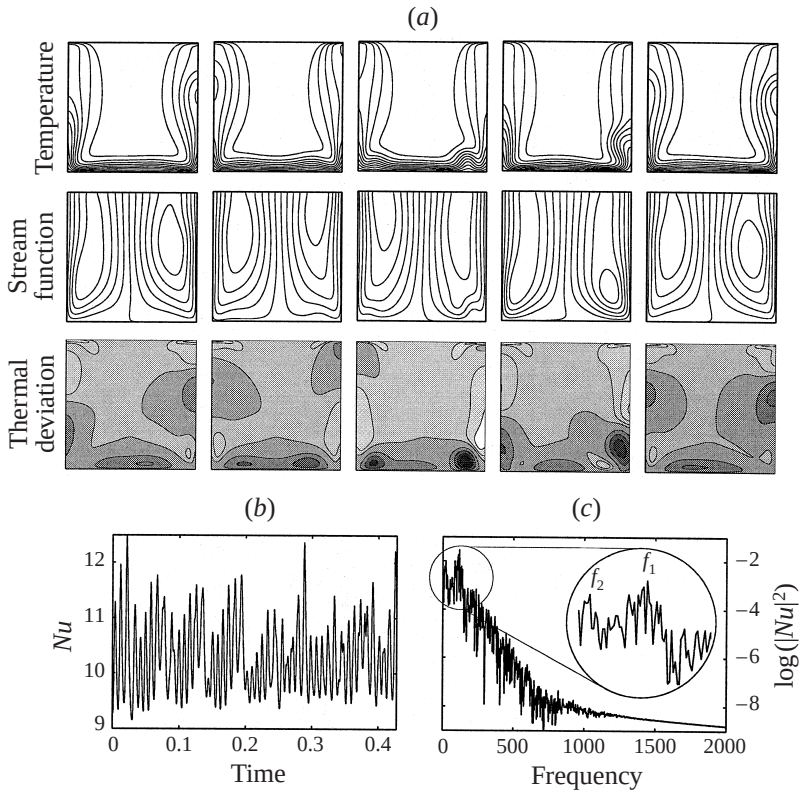

FIGURE 6. Same as figure 5 except for $Ra = 490$. Maximum thermal anomalies in (*a*) correspond to a temperature difference of 0.51. Unsteady convection is not in the single-periodic regime anymore. Noise in the spectrum signals the onset of chaotic patterns. Two incommensurate frequencies $f_1 = 130.8$ and $f_2 = 18.9$ remain identifiable.

the amplitude of the variations in the Nusselt number increases to 32% of the mean (figure 6*b*). Although two incommensurate frequencies $f_1 = 130.8$ and $f_2 = 18.9$ remain identifiable at $Ra = 490$ (figure 6*c*), a strong broadband noise in the spectrum, characteristic of non-periodic motion (Gollub & Benson 1980; Baker & Gollub 1996), suggests that convection is already in the chaotic regime.

At $Ra = 500$ (figure 7), the instabilities can at times extend above half the height of the porous layer. The amplitude of the variations in the heat transport resulting from the larger instabilities reaches up to 52% of the mean (figure 7*b*). No single frequency clearly prevails in the power spectrum (figure 7*c*). The convective regime is now chaotic. Qualitatively, however, the flow patterns appear to follow a recurrent cycle where instabilities, first infinitesimal, grow larger after each oscillation up to the point where they can flow up against the downwelling flow. This pattern repeats itself with the larger instabilities flowing intermittently to the right and to the left without any specific regularity.

4.4. *Fourth transition: unsteady-to-steady bifurcation from* $A = \frac{1}{2}$ *to* $A = \frac{1}{4}$

Above $Ra = 510$, the instabilities become large enough to flow straight up from the centre of the boundary layer and travel all the way across the porous layer (figure 8*a*). A new upwelling site is then established and the four-cell convective pattern becomes steady. The results shown in figure 8 were computed for $Ra = 550$ with an initial

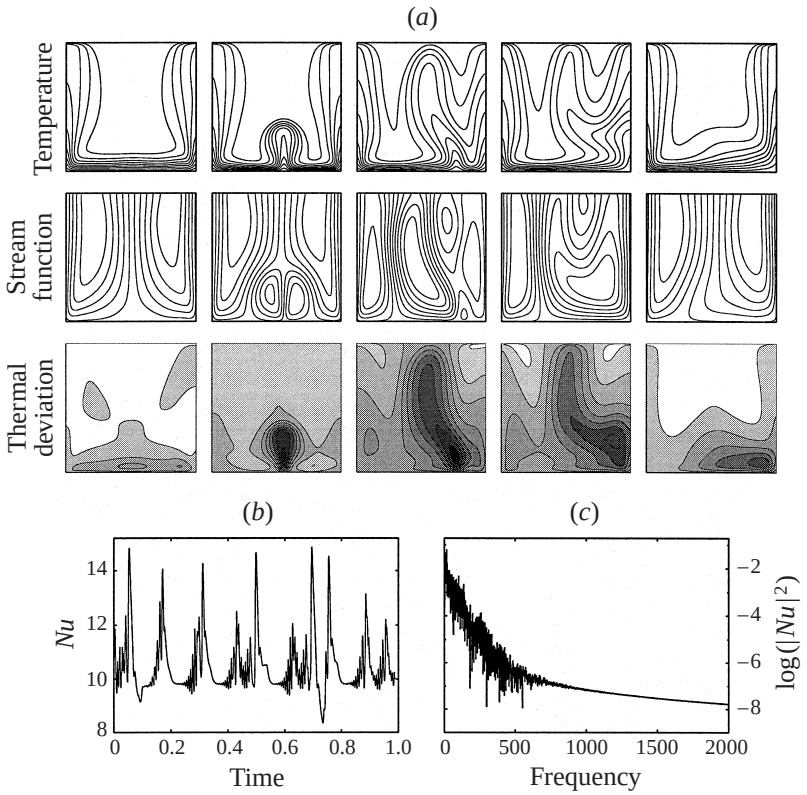

FIGURE 7. Same as figure 5 except for $Ra = 500$. Maximum anomalies contoured in (*a*) correspond to a temperature difference of 0.67. No single frequency prevails in the spectrum anymore. Unsteady convection is in the chaotic regime.

solution taken at $Ra = 500$. Similar evolutions to a steady four-cell pattern occur with any initial solution taken below $Ra = 500$, even in the monocellular range below $Ra = 107.8$. However, this transition only exists in the direction of increasing Rayleigh numbers. We computed solutions for $Ra = 300$, 450 and 480 starting with the steady quadricellular solution at $Ra = 700$. The solution for $Ra = 450$ and 480 displayed steady four-cell patterns. The solution for $Ra = 450$ and 480 displayed steady four-cell patterns. The solution for $Ra = 300$ evolved to a steady bi-cellular pattern. The reverse transition from $A = \frac{1}{4}$ to $A = \frac{1}{2}$ is therefore a steady-to-steady bifurcation and seems to occur around $Ra = 420$.

Above $Ra = 500$, the evolution along the quadri-cellular branch is similar to previous branches (figure 2). The thermal boundary layer thins while upwelling plumes narrow. As the Rayleigh number increases, the rate of increase of the Nusselt number declines while the kinetic energy increases at a near-constant rate of change (figure 3*c*).

4.5. *Fifth transition: steady-to-unsteady bifurcation at* $A = \frac{1}{4}$

Time-dependent solutions show that the convective patterns become unsteady again above $Ra \approx 970$. Interactions between instabilities born to the left and to the right of the centre plume now complicate the temporal behaviour of the system. For instance, at $Ra = 1000$, left- and right-flowing instabilities reach the centre plume with an almost opposite phase lag (with respect to the sign of the temperature anomaly)

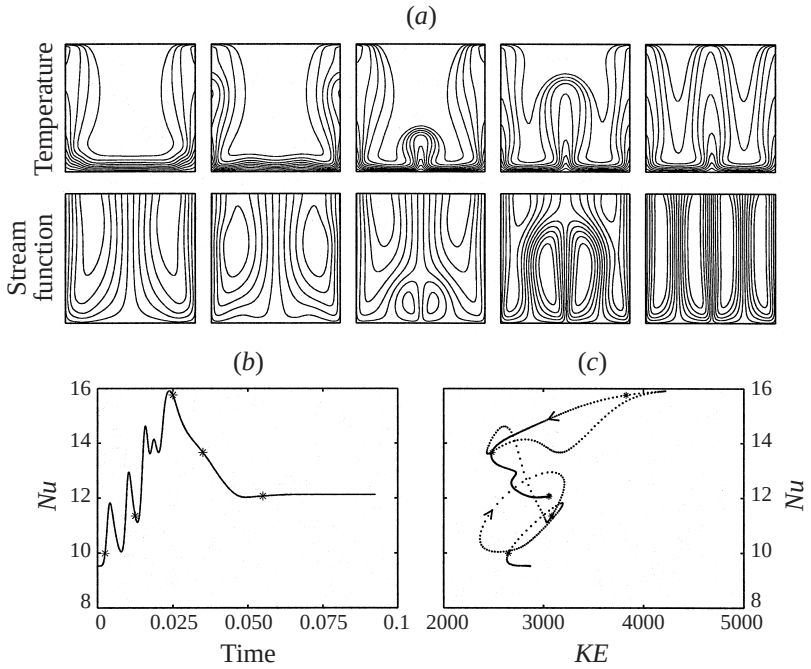

FIGURE 8. Evolution from an unsteady two-cell convection pattern at $Ra = 500$ to a four-cell steady pattern at $Ra = 550$. (*a*) Snapshots of the temperature and the stream function. Contouring is identical to figure 4. (*b*) Nusselt number as a function of time. (*c*) Nusselt number as a function of the total kinetic energy. The stars mark the location of the snapshots.

thus cancelling each other out, leaving the centre plume almost undisturbed over the top half of the porous layer (figure 9*a*). At this stage the amplitude of the resulting oscillations in the Nusselt number reach up to 4% of the mean (figure 9*b*) and the spectrum displays one characteristic frequency $f_1 = 514 \pm 5$ and its harmonics (figure 9*c*). The temperatures halfway along the vertical walls display single-periodic oscillations in opposite phase, with amplitudes 90% greater than that in the centre plume since only one instability from each boundary layer reaches each sidewall.

At $Ra = 1075$, left- and right-flowing instabilities are in phase (figure 10*a*), resulting in larger oscillations in the temperature along the centre plume. The amplitude of oscillations in the centre plume is comparable to that in the side half-plumes. The amplitude of oscillations in the Nusselt number reach 26% of the mean (figure 10*b*) and two frequencies $f_1 = 522 \pm 4$ and $f_2 = 84 \pm 2$ are identifiable in the spectrum (figure 10*c*). The strong broadband noise suggests the system may be near the onset of chaotic motion. Above $Ra = 1090$, the convective system appears to be in a chaotic regime, with oscillations reaching amplitudes of 30% of the mean. Computations at $Ra = 1100$ suggest that a finer resolution is required but it is too expensive computationally for our algorithm.

5. Discussion

We have obtained time-independent and time-dependent solutions for two-dimensional porous convection in an open-top square box uniformly heated from below up to a Rayleigh number of 1100. Our computational approach limits us to

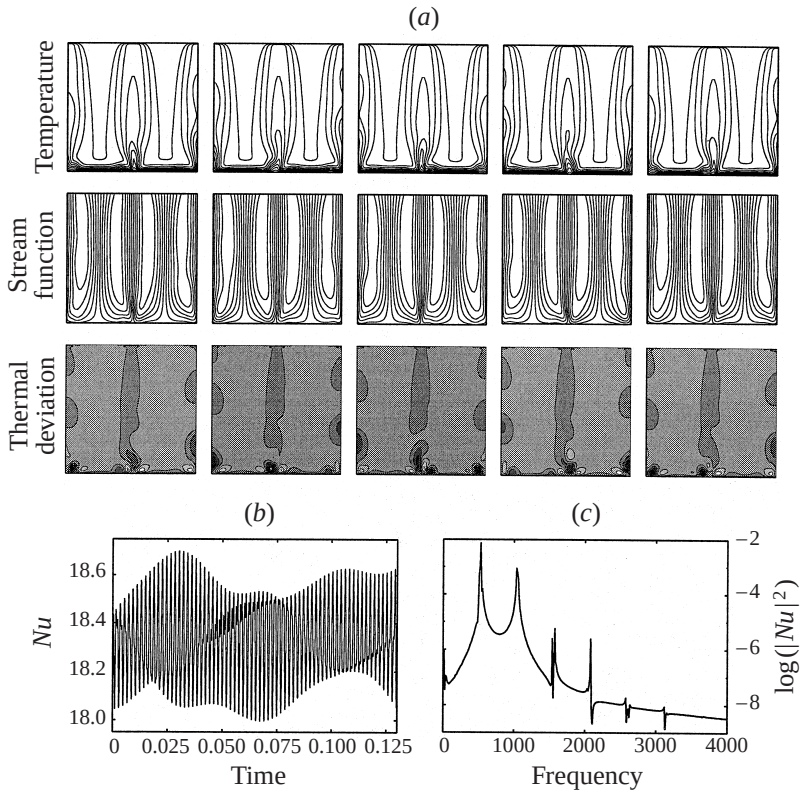

FIGURE 9. Same as figure 5 except for $Ra = 1000$. Maximum anomalies contoured in (*a*) correspond to a temperature difference of 0.26. Only one frequency $f_1 \approx 514 \pm 5$ and its harmonics appear in the power spectrum.

stable solutions only. Although we do not impose any symmetry condition, our model also seems to preclude solutions with three or five cells. We attribute this artifact to our numerical formulation. Despite these limitations, our model yields a number of interesting results. As for a confined box, unsteady convection in the open-top square box undergoes a general sequence of bifurcations, from periodic to quasi-periodic to chaotic flows. However, significant differences exist. First, stable unsteady convection does not seem to occur in the uni-cellular flow configuration. It appears only in the bi- and quadri-cellular configurations. Second, the first appearance of unsteady convection evolves over a small Rayleigh number interval from an unsteady chaotic state, to a steady higher convective mode (i.e. a convective cell with a smaller aspect ratio).

The evolution we observe is best considered in the context of the hypothesis that convective systems adopt the configuration that maximizes the heat transport (Malkus 1954). Figure 2 shows clearly that each transition is associated with an increase in the rate of increase of the Nusselt number with *Ra*. There are three transitions to higher modes. The first two, the onset of convection and the transition from mono- to bi-cellular flow patterns, are similar. They involve a one-time-only destabilization of the conductive layer and a steady-to-steady bifurcation in the flow patterns. The bifurcation Rayleigh number corresponds to the intersection of the steady-state branches. For the transition from one- to two-cell patterns an unstable

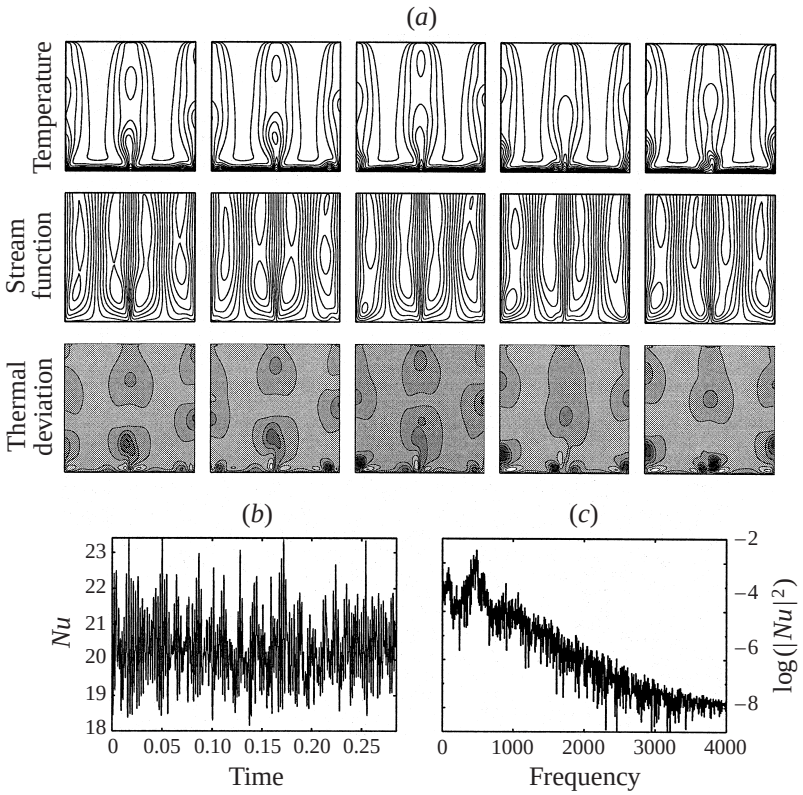

FIGURE 10. Same as figure 5 except for $Ra = 1075$. The maximum anomalies contoured in (*a*) correspond to a temperature difference of 0.36. The signal is much noisier but two incommensurate peak frequencies $f_1 \approx 522 \pm 4$ and $f_2 \approx 84 \pm 2$, exist in the power spectrum.

mixed mode may exist but is not captured by our solutions. The third transition from bi- to quadri-cellular flow patterns is preceded by a bifurcation to unsteady convection which begins at a Rayleigh number corresponding to the intersection of the steady convection branches. However, a significant hysterisis loop exists. No unsteady convection occurs in the decreasing-Ra direction. The reverse transition from quadri- to bi-cellular patterns is a steady-to-steady bifurcation and occurs around $Ra = 425$, near the intersection of the steady-state branches (figure 2). The mean Nusselt numbers for the bi-cellular unsteady convective states fall between the bi- and quadri-cellular steady branches. On the prograde branch our results violate Malkus' hypothesis which predict that the steady quadri-cellular solutions should therefore prevail past $Ra = 425$. We believe our results reflect the balance between the strength of the boundary-layer instabilities and the vigour of the overall convective flow. At low Rayleigh numbers, the weak convective flow allows a direct transition from a steady uni-cellular flow to a steady bi-cellular flow. The first boundary-layer instability to appear initiates a new upwelling site. At higher Rayleigh numbers the instabilities that develop in the boundary layer are swept away by the overall convective flow and convection is unsteady. It should be noted that Graham & Steen (1994) previously reported a counterexample to Malkus' maximal heat transport principle. They found solutions for the confined system where the Nusselt number can actually decrease with increasing Rayleigh number.

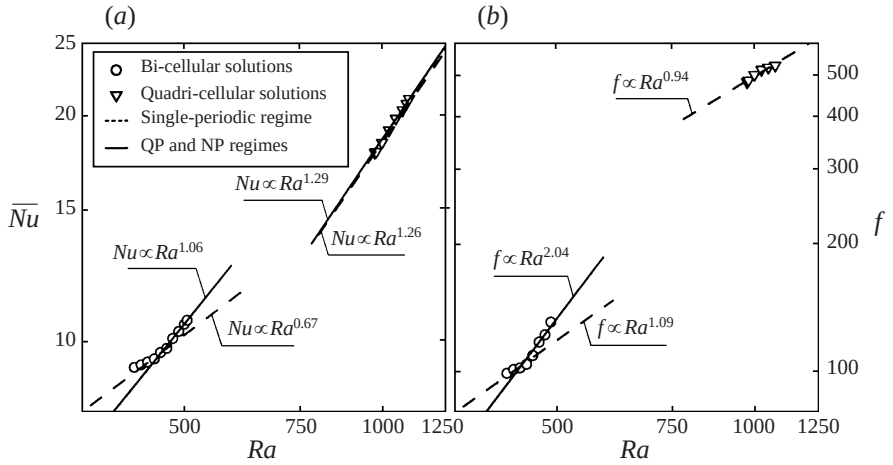

FIGURE 11. (*a*) Least-square fits to the mean Nusselt number of bi- and quadri-cellular unsteady solutions. Dashed lines show the fits to the single-periodic solutions only. Solid lines show the fits to the quasi- (QP) and non-periodic (NP) regimes. Least-square fits to all the bi- and quadri-cellular solutions yield $Nu \propto Ra^{0.81}$ and $Nu \propto Ra^{1.28}$, respectively. (*b*) Same as (*a*) but for the characteristic frequencies.

On the basis of simple physical and dimensional arguments Howard (1964) first proposed that Ra and Nu would scale asymptotically for Bénard convection at higher Rayleigh numbers as $Nu \propto Ra^{1/3}$. In the porous medium, the same analysis applies (Horne & O'Sullivan 1978; Graham & Steen 1994), but since Ra scales linearly with the height of the layer instead of cubically, the theoretical scaling law is $Nu \propto Ra$. This scaling has been observed in laboratory experiments in porous media (Elder 1967) and in Hele-Shaw cells (Koster & Muller 1982), as well as in numerical experiments of closed-top porous convection (e.g. Kimura *et al.* 1986; Graham & Steen 1994). For our results, the least-squares curve fits of the average Nusselt numbers for unsteady convection in the bi- and quadri-cellular regimes are $Nu \propto Ra^{0.81}$ and $Nu \propto Ra^{1.28}$, respectively. These scalings differ significantly from the theoretical asymptotic law. Such deviations may be attributed to the presence of vertical boundaries which quantize the wavenumber of the instabilities born in the boundary layer (Graham & Steen 1994).

Schubert & Straus (1982) and Kimura *et al.* (1986) show that, in a closed-top box, $Nu \propto Ra^{2/3}$ in the first single-periodic regime, while $Nu \propto Ra^{11/10}$ after that. Thermal plumes form when the small instabilities grow large enough to move fluid out of the boundary layer before they reach the downstream end of the layer. Graham & Steen (1994) define a plume as having formed when the isotherms contouring the boundary layer instabilities become nearly vertical away from the downstream corner. They find that the onset of the Howard scaling corresponds to the onset of plume formation in the confined geometry.

We apply separate least-square fits to the first single-periodic regimes and the subsequent quasi-periodic (QP) and non-periodic (NP) regimes (figure 11). For Ra in the single-periodic regime ($Ra < 480$) of the bi-cellular solutions $Nu \propto Ra^{0.67}$. Above, in the quasi- and non-periodic regime of the bi-cellular solutions $Nu \propto Ra^{1.06}$, matching closely the theoretical scaling. According to the operational definition of Graham & Steen (1994), the onset of plume formation in the unsteady bi-cellular solutions occurs just above $Ra = 490$. As for the confined geometry, the onset of

the Howard scaling in the open-top configuration appears to correspond to the onset of plume formation. The single-periodic regime is characterized by small fluctuations born in the centre of the boundary layer growing as they are convected across the horizontal isothermal surfaces. The associated characteristic frequencies validate this general picture (figure 11*b*). In the bi-cellular solutions, the frequencies scale closely to the theoretical scaling $f \propto Ra^2$ for the QP and NP regime only. In the single-periodic regime, the frequencies scale near $f \propto Ra$ which corresponds to the characteristic sweep timescale across the porous box.

A least-squares fit to the quadri-cellular solutions yields $Nu \propto Ra^{1.26}$ in the single-periodic regime and $Nu \propto Ra^{1.29}$ in the subsequent quasi-periodic regime (figure 11*a*). We do not observe thermal plumes in any of these regimes. The timescale of formation of boundary layer instabilities seems to follow the sweep scale of the general convective flow (figure 11*b*), suggesting that our quadri-cellular solutions do not attain the onset of Howard's high Rayleigh number scaling.

While the appearance of unsteadiness in the bi-cellular solutions coincides with the intersection of the steady bi- and quadri-cellular branches, unsteady convection appears in the quadri-cellular solutions at $Ra = 975$, well before the intersection of the quadri- and hexa-cellular branches ($Ra \approx 1125$). Since the rate of increase of the average Nusselt number past the onset of quadri-cellular unsteady convection is higher than that for the steady hexa-cellular branch (figure 2), we suspect that the four-cell pattern is the maximum stable convection mode in the open-top square configuration and that above $Ra = 1100$ the system conserves a four-cell unsteady pattern which evolves to chaotic flow.

6. Conclusions

The objective of this study was to determine the evolution with Rayleigh number of flow and heat transport in an open-top square porous layer. The results show significant differences from the evolution in a confined square box (e.g. Kimura *et al.* 1986; Caltagirone & Fabrie 1989). First, uni-cellular convection is limited to Rayleigh numbers less than 107.8 and the systems quickly evolves to bi- then quasi-cellular convection as the Rayleigh number increases. Second, stable unsteady convection precedes the transition from bi-cellular to quadri-cellular convective patterns but not from mono- to bi-cellular patterns. In the bi-cellular patterns, unsteady convection is limited to a small Rayleigh number range 425–505 and only appears when the convective system evolves from a two-cell pattern at lower Rayleigh numbers. In the decreasing Rayleigh number direction, solutions in the range 425–505 display a steady four-cell pattern, thus producing an important hysterisis loop. In this range, and also in the range 975–1100 for the quadri-cellular configuration, unsteady flow and heat transport display a sequence of bifurcations from periodic to quasi-periodic to chaotic patterns similar to that observed in a confined square box. Transitions to higher convective modes can only occur when the boundary-layer instabilities are stronger than the vigour of the overall convective flow. Otherwise, unsteady convection occurs. All the bifurcations in the flow, whether transitions to higher convective modes or transitions to unsteady flow, are associated with increases in the average heat transport. The onset of the theoretical boundary scaling $Nu \propto Ra$ corresponds to the onset of plume formation in the bi-cellular solutions. Our quadri-cellular solutions do no reach the onset of Howard's scaling. Finally, our results suggest that the maximum stable convection mode in the open-top square configuration is a four-cell flow pattern.

This work was supported by a Fulbright Fellowship award to A. S. M. Cherkaoui and by the National Science Foundation under grant OCE-9629425. We thank Peter J. Schmid for useful discussions and three anonymous referees for thorough reviews.

REFERENCES

Aidun, C. K. 1987 Stability of convection rolls in porous media. *ASME Heat Transfer Div.* **94**, 31–36.

Aidun, C. K. & Steen, P. H. 1987 Transition of oscillatory convective heat transfer in a fluid-saturated porous medium. *J. Thermophys. Heat Transfer* **1**, 268–273.

Baker, G. L. & Gollub, J. P. 1996 *Chaotic Dynamics: An Introduction.* Cambridge University Press.

Bear, J. 1972 *Dynamics of Fluids in Porous Media.* Elsevier.

Caltagirone, J. P. 1975 Thermoconvective instabilities in a horizontal porous layer. *J. Fluid Mech.* **72**, 269–287.

Caltagirone, J. P., Cloupeau, M. & Combarnous, M. 1971 Convection naturelle fluctuante dans une couche poreuse horizontale. *C. R. Acad. Sci. Paris* **273 B**, 833–836.

Caltagirone, J. P. & Fabrie, P. 1989 Natural convection in a porous medium at high Rayleigh numbers Part I – Darcy's model. *Eur. J. Mech.* B/*Fluids* **8**, 207–227.

Caltagirone, J. P., Fabrie, P. & Combarnous, M. 1987 De la convection naturelle oscillante en milieu poreux au chaos temporel? *C. R. Acad. Sci.* II **305**, 549–553.

Cherkaoui, A. S. M., Wilcock, W. S. D. & Baker, E. T. 1997 Thermal fluxes associated with the 1993 diking event on the CoAxial segment, Juan de Fuca Ridge: A model for the convective cooling of a dike. *J. Geophys. Res.* **102**, 24887–24902.

Combarnous, M. & LeFur, B. 1969 Transfer de chaleur par convection naturelle dans une couche poreuse horizontale. *C. R. Acad. Sci. Paris* **269 B**, 1009.

Donaldson, I. G. 1962 Temperature gradients in the upper layers of the Earth's crust due to convective water flow. *J. Geophys. Res.* **67**, 3449–3459.

Elder, J. W. 1967 Steady free convection in a porous medium heated below. *J. Fluid Mech.* **27**, 29–48.

Fisher, A. T. 1998 Permeability within basaltic oceanic crust. *Rev. Geophys.* **36**, 143–182.

Gollub, J. P., & Benson, S. V. 1980 Many routes to turbulent convection. *J. Fluid Mech.* **100**, 449–470.

Graham, M. D., Muller, U. & Steen, P. H. 1992 Time-periodic thermal convection in Hele-Shaw cell slots: The diagonal oscillation. *Phys. Fluids* A **4**, 2382–2393.

Graham, M. D. & Steen, P. H. 1992 Strongly interacting traveling waves and quasiperiodic dynamics in porous media convection. *Physica* D **54**, 331–350.

Graham, M. D. & Steen, P. H. 1994 Plume formation and resonant bifurcations in porous-media convection. *J. Fluid Mech.* **272**, 67–89.

Haymon, R. M. 1996 The response of ridge-crest hydrothermal systems to segmented episodic magma supply. In *Tectonic, Magmatic, Hydrothermal, and Biological Segmentation of Mid-Ocean Ridges* (ed. C. J. MacLeod, P. A. Taylor & C. L. Walker), pp. 157–168.

Horne, R. N. & Caltagirone, J. P. 1980 On the evaluation of thermal disturbances during natural convection in a porous medium. *J. Fluid Mech.* **100**, 385–395.

Horne, R. N. & O'Sullivan, M. J. 1974 Oscillatory convection in a porous medium heated from below. *J. Fluid Mech.* **66**, 339–352.

Horne, R. N. & O'Sullivan, M. J. 1978 Origin of oscillatory convection in a porous medium heated from below. *Phys. Fluids* **21**, 1260–1264.

Howard, L. N. 1964 Convection at high Rayleigh number. In *Applied Mechanics* (ed. H. Görtler), *Proc. 11th Congr. Appl. Mech.*, pp. 1109–1115.

Kimura, S., Schubert, G. & Straus, J. M. 1986 Route to chaos in porous-medium thermal convection. *J. Fluid Mech.* **116**, 305–324.

Koster, J. N. 1982 Heat transfer in vertical gaps. *Intl J. Heat Mass Trans.* **25**, 426–428.

Koster, J. N. 1988 Interaction of local instabilities during oscillatory convection. *Phys. Rev.* A **37**, 3410–3422.

Koster, J. N. & Muller, U. 1982 Free convection in vertical gaps. *J. Fluid Mech.* **125**, 429–451.

Koster, J. N. & Muller, U. 1984 Oscillatory convection in vertical slots. *J. Fluid Mech.* **139**, 363–390.

Lennie, T. B., McKenzie, D. P., Moore, D. R. & Weiss, N. O. 1988 The breakdown of steady convection. *J. Fluid Mech.* **188**, 47–85.

Lister, C. R. B. 1981 Rock and water histories during sub-oceanic hydrothermal events. *Oceanologica Acta* **4**, C4, 41–46.

Lyubimov, D. V., Putin, G. F. & Chernatynskii, V. I. 1977 On convection motions in a Hele-Shaw cell. *Sov. Phys. Dokl.* **22**, 360–362.

Malkus, W. V. R. 1954 The heat transport and spectrum of thermal turbulence. *Proc. R. Soc. Lond.* A **225**, 196–212.

Nield, D. A. 1968 Onset of thermohaline convection in a porous medium. *Water Resources Res.* **4**, 553–560.

Nield, D. A. & Bejan, A. 1992 *Convection in Porous Media.* Springer.

Patankar, S. V. 1980 *Numerical Heat Transfer and Fluid Flow*. Hemisphere.

Patankar, S. V. 1981 A calculation procedure for two-dimensional elliptic situations. *Numer. Heat Transfer* **4**, 409–425.

Ribando, T. K., Torrance, K. E. & Turcotte, D. L. 1976 Numerical models for hydrothermal circulation in the oceanic crust. *J. Geophys. Res.* **81**, 3007–3012.

Rosenberg, N. D. 1991 Numerical studies of fluid flow and heat transport in hydrothermal systems. PhD thesis, University of California.

Schubert, G. & Straus, J. M. 1982 Transitions in time-dependent thermal convection in fluid-saturated porous media. *J. Fluid Mech.* **121**, 301–313.

Steen, P. H. & Aidun, C. K. 1988 Time-periodic convection in porous media: transition mechanism. *J. Fluid Mech.* **196**, 263–290.

Stein, C. A. & Stein, S. 1994 Constraints on hydrothermal heat flux through the oceanic lithosphere from global heat flow. *J. Geophys. Res.* **99**, 3081–3095.

Wilcock, W. S. D. & Delaney, J. R. 1996 Mid-ocean ridge sulfide deposits: Evidence for heat extraction from magma chambers or cracking fronts? *Earth Planet. Sci. Lett.* **145**, 49–64.

Williams, J. G. & Von Herzen, R. P. 1986 Heat loss from the Earth: New estimate. *Geology* **2**, 327–328.